Geodetic and geophysical results from a Taiwan airborne gravity survey: Data reduction and accuracy assessment

Cheinway Hwang,[1] Yu-Shen Hsiao,[1] Hsuan-Chang Shih,[1] Ming Yang,[2] Kwo-Hwa Chen,[3] Rene Forsberg,[4] and Arne V. Olesen[4]

Received 15 December 2005; revised 28 August 2006; accepted 29 December 2006; published 17 April 2007.

[1] An airborne gravity survey was conducted over Taiwan using a LaCoste and Romberg (LCR) System II air-sea gravimeter with gravity and global positioning system (GPS) data sampled at 1 Hz. The aircraft trajectories were determined using a GPS network kinematic adjustment relative to eight GPS tracking stations. Long-wavelength errors in position are reduced when doing numerical differentiations for velocity and acceleration. A procedure for computing resolvable wavelength of error-free airborne gravimetry is derived. The accuracy requirements of position, velocity, and accelerations for a 1-mgal accuracy in gravity anomaly are derived. GPS will fulfill these requirements except for vertical acceleration. An iterative Gaussian filter is used to reduce errors in vertical acceleration. A compromising filter width for noise reduction and gravity detail is 150 s. The airborne gravity anomalies are compared with surface values, and large differences are found over high mountains where the gravity field is rough and surface data density is low. The root mean square (RMS) crossover differences before and after a bias-only adjustment are 4.92 and 2.88 mgal, the latter corresponding to a 2-mgal standard error in gravity anomaly. Repeatability analyses at two survey lines suggest that GPS is the dominating factor affecting the repeatability. Fourier transform and least-squares collocation are used for downward continuation, and the latter produces a better result. Two geoid models are computed, one using airborne and surface gravity data and the other using surface data only, and the former yields a better agreement with the GPS-derived geoidal heights. Bouguer anomalies derived from airborne gravity by a rigorous numerical integration reveal important tectonic features.

Citation: Hwang, C., Y.-S. Hsiao, H.-C. Shih, M. Yang, K.-H. Chen, R. Forsberg, and A. V. Olesen (2007), Geodetic and geophysical results from a Taiwan airborne gravity survey: Data reduction and accuracy assessment, *J. Geophys. Res.*, *112*, B04407, doi:10.1029/2005JB004220.

1. Introduction

[2] Taiwan's terrain is complex and mostly inaccessible for gravity survey. Over 75% of Taiwan's terrain is covered with hills and high mountains, with the highest point being nearly 4000 m (Figure 1). The variation of gravity anomaly over the region is large, ranging from about −400 mgal over the trench east of Taiwan to 400 mgal over the Central Range of Taiwan. Here the existing gravity data are sparsely distributed, and there are uncertainties in the gravity datum and the coordinate system associated with point gravity data [*Hwang*, 1997]. For such applications as geoid modeling, vertical datum determination, geological study, and ocean current determination, a dense, accurate gravity data set is needed. To this end, Ministry of the Interior (MOI) of Taiwan sponsored an airborne gravity survey over the period of May 2004 to May 2005. The field work and data reduction were carried out by the National Chiao Tung University (NCTU), Taiwan, and the National Survey and Cadastre (KMS), Denmark. The survey area covers the entire Taiwan Island and its offshore waters.

[3] There are many regions in the world where airborne gravity surveys have been carried out [see, e.g., *Wei and Schwarz*, 1998; *Bell et al.*, 1999; *Olesen et al.*, 2000; *Forsberg and Solheim*, 2000; *Childers et al.*, 2001; *Forsberg et al.*, 2003; *Verdun et al.*, 2003]. The Taiwan airborne gravity survey described in this paper will be just one such survey. However, for a best result from an airborne gravity survey, many issues need to be investigated [*Schwarz and Li*, 1997]. These issues are largely related to the kinematic positioning of aircraft by global positioning system (GPS), error models of measurement system, filtering, downward continuation, and methods for geoidal and geophysical models using airborne and other gravity data. These issues are still under extensive investigations today, and the ultimate

[1]Department of Civil Engineering, National Chiao Tung University, Hsinchu, Taiwan.
[2]Department of Geomatics, National Cheng Kung University, Tainan, Taiwan.
[3]Department of Real Estate and Built Environment, Taipei University, Taipei, Taiwan.
[4]Danish National Space Center, Copenhagen, Denmark.

0148-0227/07/2005JB004220$09.00

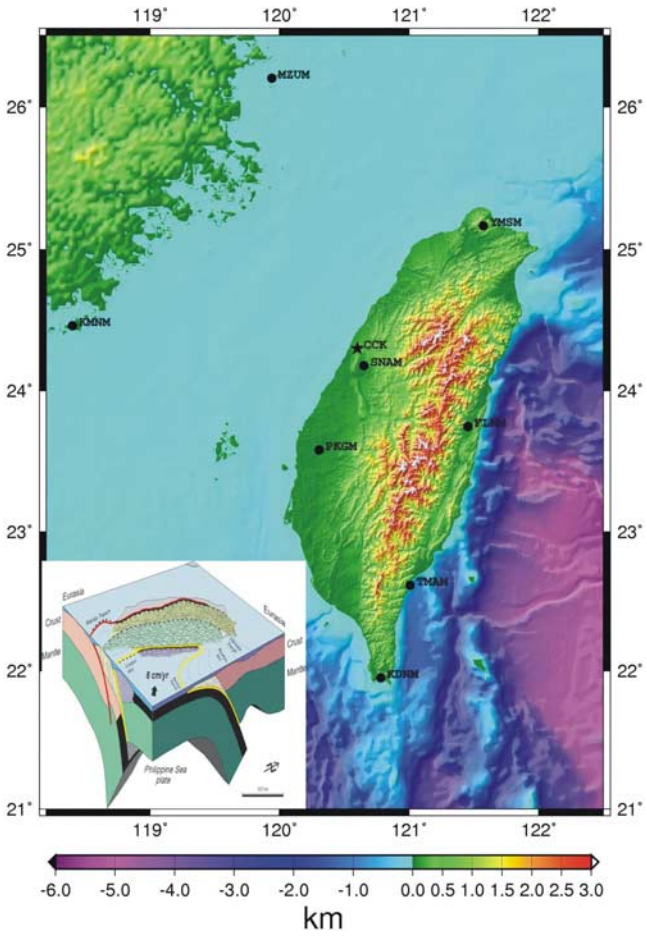

Figure 1. Terrain and bathymetry around Taiwan and GPS tracking stations (solid circles) for precise aircraft positioning. Star shows the Taichung (CCK) Airport where the King-Air Beechcraft-200 is based. Inserted is a tectonic map of Taiwan from *Angelier et al.* [1997]. The subduction of the Philippine Sea Plate into the Eurasia Plate creates a deep trench and large, negative gravity anomalies east of Taiwan. Mass surplus in the mountains results in positive gravity anomalies (Figure 3).

goal is to find the best solutions to these problems. Therefore the objective of this paper is to derive the best geodetic and geophysical results from the Taiwan airborne gravity data while focusing on the following issues: (1) accuracies of GPS-derived position, velocity, and acceleration; (2) achievable accuracy and spatial resolution of airborne gravity data; and (3) methods for data reductions and applications to downward continuation, geoid modeling, and Bouguer anomaly modeling.

2. Taiwan Airborne Gravity Survey

[4] Since Taiwan is long in the north-south direction and short in the west-east direction (Figure 1), most of the flight lines should be in the north-south direction to avoid excessive turns of flight and to reduce unusable data in the beginning section of a line. On the basis of this consideration, the numbers of planned survey lines in the north-south, east-west, northeast-southwest, and northwest-southeast directions are 64, 22, 10, and 6, respectively. The cross-line spacing is 4.5 km for all survey lines, except the east-west lines, which are spaced at 20 km. The west-east lines are mainly for crossover analyses. The cross-line spacing of 4.5 km is approximately equal to the theoretical resolvable wavelength of gravity anomaly at the flight altitude (see section 4). A LaCoste and Romberg (LCR) System II air-sea gravimeter (serial number: S-133) was used to collect the airborne gravity data. This gravimeter has a nominal resolution of 0.01 mgal and an accuracy of better than 1 mgal [*L&R Air-Sea Gravity System II*, 2003]. It uses spring tension and beam velocity measurements to obtain relative gravity variations. A King-Air Beechcraft-200 aircraft was modified to accommodate this gravimeter. The speed of flight is 306 km/hour relative to the surface, and the average altitude is 5156 m. Both the airborne gravimeter and aircraft are owned by MOI. Furthermore, the decision of the survey plan was based on the allocated time of the King-Air Beechcraft-200 (support of other missions), Taiwan's terrain (highest point, 3952 m), project duration (1 year), and a political factor (not to over the center of the Taiwan Strait).

[5] The King-Air Beechcraft-200 is equipped with a Trimble 5700 GPS receiver sampling data at 1 Hz. For the kinematic positioning of the aircraft, GPS data at seven permanent GPS tracking stations around Taiwan and one tracking station (SNAM, see Figure 1) near the Taichung airport were collected. The gravity readings were sampled at 1 Hz, corresponding to an 85-m sampling interval on the surface. The gravity value at the aircraft parking spot was determined using relative gravity measurements collected by a Graviton-EG gravimeter, and it is tied to the gravity value at the Taichung FG5 absolute gravity station. The standard error of this gravity value is 0.04 mgal based on a relative gravity network adjustment. The Taiwan airborne gravity survey was carried out from May 2004 to March 2005. In total, we collected 43 days of gravity and GPS data, including 3 days of reflights at the survey lines with bad data. The number of flight hours is more than 200.

3. GPS Positioning of Aircraft

3.1. Kinematic GPS Positioning

[6] Precise aircraft position, velocity, and acceleration are critical to the success of an airborne gravity survey [*Schwarz and Li*, 1997; *Kennedy et al.*, 2002]. In this paper, the trajectories of the aircraft were determined in two kinematic solutions: (1) GPSurvey solution, using the broadcast ephemeris of GPS, and (2) Bernese 5.0 solution [*Beutler et al.*, 2004], using the International GPS Service (IGS) precise ephemeris of GPS [*Kouba*, 2003]. GPSurvey is a commercial software and has been used in many airborne survey data reductions [e.g., *Forsberg et al.*, 2003; *Olesen*, 2003]. The Bernese software has been used by *Verdun et al.* [2003]. The GPSurvey solution provided aircraft coordinates relative to the GPS station at the airport (SNAM in Figure 1) and is considered an initial solution. The result from the GPSurvey solution was used to assess the quality of airborne gravity data along a survey line and to decide whether a reflight is necessary. In general, flights carried out in cloudy or rainy day produce bad gravity data. This is due to turbulence that generates large vertical

accelerations (this is seen in accelerations from GPSurvey and gravimeter readings occurring at the same time) that almost totally obscure the gravity signal. After each flight, we computed the differences between airborne gravity values from the GPSurvey solution and those from the upward continuation of surface data (section 6.1). For a "bad" survey line, the differences are very large at most points (exceeding 10 mgal). On the basis of a visual inspection of such differences and GPS accelerations along a survey line, we empirically decide to adopt or reject the result of this line. With a line accepted, the final GPS solution was obtained by Bernese and this was carried out after several weeks of data collection.

[7] For the fixed coordinates of the eight tracking stations (Figure 1) that are used to constrain the aircraft positioning, we did not use the published coordinates of MOI because of the uncertainties in the models of land deformation and local plate tectonics in Taiwan. Instead, we first determined the coordinates of the eight tracking stations in a network adjustment using 1 day of GPS observations by holding the coordinates of YMSM fixed. Such coordinates are free from the uncertainties of land deformation and plate motion and have an accuracy at the centimeter level.

[8] In the kinematic positioning with Bernese, a number of parameters contained in the double-differenced phase observations were estimated together with the aircraft's positions. The unknown parameters are solved in a least-squares batch process [*Beutler et al.*, 2004]. These parameters are grouped into two subsets in the normal equations:

$$\begin{bmatrix} \mathbf{N}_{11} & \mathbf{N}_{12} \\ \mathbf{N}_{21} & \mathbf{N}_{22} \end{bmatrix} \begin{bmatrix} \mathbf{X}_1 \\ \mathbf{X}_2 \end{bmatrix} = \begin{bmatrix} \mathbf{C}_1 \\ \mathbf{C}_2 \end{bmatrix} \tag{1}$$

where $\mathbf{N}_{ij}$, $\mathbf{C}_i$, $i = 1, 2$ are submatrices of the normal equations; subset $\mathbf{x}_1$ contains ground station coordinates, tropospheric parameters, and phase ambiguities; and subset $\mathbf{x}_2$ contains epoch-by-epoch kinematic positions of the moving platform. Subset $\mathbf{x}_1$ is first solved as

$$\mathbf{x}_1 = \left(\mathbf{N}_{11} - \mathbf{N}_{12}\mathbf{N}_{22}^{-1}\mathbf{N}_{21}\right)^{-1}\left(\mathbf{c}_1 - \mathbf{N}_{12}\mathbf{N}_{22}^{-1}\mathbf{c}_2\right) \tag{2}$$

Subset $\mathbf{x}_2$ is then obtained by the forward substitution

$$\mathbf{x}_2 = \mathbf{N}_{22}^{-1}(\mathbf{c}_2 - \mathbf{N}_{21}\mathbf{x}_1) \tag{3}$$

[9] In the solution, the standard stochastic model of GPS phase observables was used [*Seeber*, 2003]. Kinematic positioning is similar in many ways to static positioning. For example, GPS phase ambiguities are treated as constants for continuous data spans. One correction parameter per station per hour was estimated to absorb the residual tropospheric delay. In order to remove the first-order ionospheric effect, we formed the ionosphere-free (L3) phase observables by combining the L1 and L2 phase data, and held fixed the IGS GPS satellite orbits. Unlike the land-based static application, different coordinate parameters have to be set up for each epoch because of the rapid change of the aircraft's position. Therefore the degree of freedom and positioning accuracy associated with long-range kinematic solutions are generally less than those of the static case. Furthermore, to achieve a best result of kinematic positioning, we used a kinematic network solution. In this case, double-differenced phase observables between the aircraft and the eight tracking stations were formed and used to obtain the final coordinates. Initial values for the kinematic positions (parameter subset $\mathbf{x}_2$) are required for linearization of the nonlinear GPS observation equations. Moreover, if good a priori values with small uncertainties for $\mathbf{x}_2$ are available, naturally, better final results for $\mathbf{x}_2$ (and consequently $\mathbf{x}_1$) can be obtained. In this paper, point positioning with smoothed pseudorange measurements is used to obtain adequate a priori values to the satisfactory level. To derive aircraft's velocity and acceleration at epoch, the positional data before and after this epoch are first fitted by a polynomial. It was found that a polynomial obtained from a 14-point fit produces the best result. Differentiation of the fitting polynomial then yields velocity and acceleration; the detail is described in the work of *Hwang et al.* [2006].

3.2. Accuracy Assessment of Aircraft Position, Velocity, and Acceleration

[10] Here we only assess the accuracy of the Bernese solution. We select 10 sessions of airborne GPS data for the assessment. Each session of about 4 hours in data length was divided into two independently processed subsessions with a 30-min overlap. The 10 overlapping sessions were selected so that the tracks of the overlaps cover coastal plains, high mountains, and oceans. Figure 2a shows a typical example of position differences in an overlapping session, which vary slowly and contain spikes and discontinuities. Figure 2b shows that the power spectral density (PSD) of position differences for the three components is reddened. The spectral index, i.e., the value of the exponent x in $S(f) \approx f^x$, where S is PSD and f is frequency, is -0.7, -0.8, and -1.4 for the north, east, and vertical components, respectively. Therefore the PSD approximately indicates flicker noise ($x = -1$) for the north and east components and a combination of flicker noise and a random-walk process ($x = -2$) for the vertical component. Thus the overlapping differences of position estimates are dominated by the long-wavelength errors in GPS positioning. These results are consistent with other studies [e.g., *Verdun et al.*, 2003] and represent the combined effect of long- and short-wavelength GPS errors. Furthermore, values of the PSD of the vertical component are 0.5 to 1.5 orders of magnitude smaller than the PSD of the north component but are similar to the PSD of the east component at high frequencies. Values of the PSD of the north component are 2 to 4 orders of magnitude smaller than the east component at all frequencies.

[11] The overlapping difference can be regarded as the internal accuracy of GPS positioning. It was found that spikes and discontinuities were associated with phase ambiguity changes, i.e., change of visible satellites and/or cycle slips in one or more of the baselines. The position differences in Figure 2a are mainly caused by the differences in the estimated common parameters associated with the overlapping subsessions, for example, phase ambiguities and tropospheric parameters. Since these common parameters will remain unchanged within a certain time span, their effects will be reduced upon differentiation. That is, we

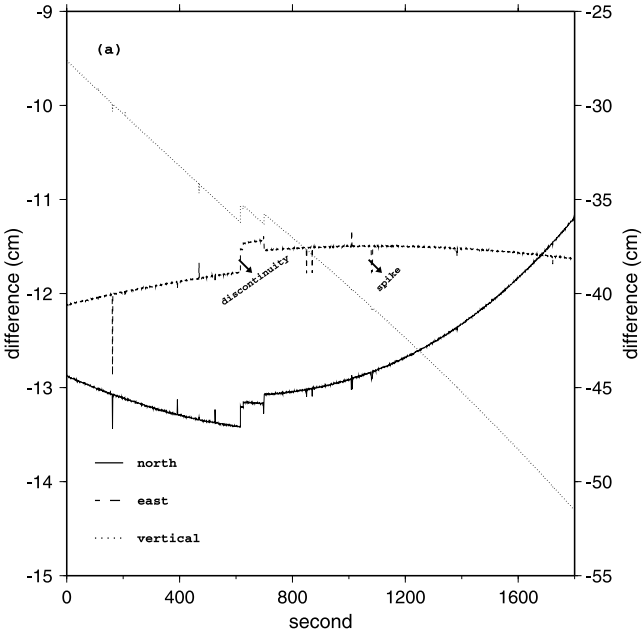

Figure 2. (a) Differences of position at an overlapping session on 15 November 2004 in the north, east, and vertical components. The left vertical scale is for the north and east components, and the right vertical scale is for the vertical component. Discontinuities occur at seconds 615 and 699. (b) Power-spectral densities of the differences.

would expect that the differences in position-derived velocity and acceleration (by numerical differentiation) are less affected by the differences in common parameters. Table 1 lists the average root mean square (RMS) differences in position, velocity, and acceleration from the 10 overlapping sessions. The overall positioning accuracy is of the order of decimeter, with the vertical component being the largest. Table 1 indicates that the long-wavelength positioning error does not propagate to the errors in velocity and acceleration. This is explained as follows. Let velocity and acceleration be approximated as

$$\begin{aligned} v_h &\approx \frac{\Delta p}{\Delta t} \\ v_z &= \frac{\Delta z}{\Delta t} \\ a_z &\approx \frac{\mathrm{D}v_z}{\Delta t} \end{aligned} \tag{4}$$

where $\Delta t = 1$ s (for an 1-Hz sampling interval), and Δp, Δz, and Δv_z are differences in along-line horizontal distance, height, and vertical velocity, respectively, between two consecutive data points. Assume that the RMS differences in Table 1 are equal to the standard errors of the respective quantities. In theory, a standard error of 0.293 m (Table 1) in vertical position will translate to a standard error of $0.293 \times \sqrt{2} = 0.414$ ms^{-1} in vertical velocity and $0.414 \times \sqrt{2} = 0.585$ ms^{-2} in vertical acceleration. However, the standard errors in Table 1 are much smaller than these two numbers. This implies that the differentiation of positions does reduce the effects of long-wavelength errors of positions on velocity and acceleration (see also the discussion by *Verdun et al.* [2003] and discussion in section 5).

4. Theoretical Resolvable Wavelength at Flight Altitude

[12] The achievable spatial resolution of airborne gravimetry depends on data noise and flight altitude. It is known that gravity signal will be attenuated at the flight altitude [*Torge*, 1989, p. 287]. Such attenuation is now discussed, and a theory of resolvable wavelength at a given flight altitude is presented below. This theory is based on the concept of average power of acceleration in satellite gravimetry [*Hwang and Lin*, 1998]. First, gravity anomaly can be expanded into a series of spherical harmonics as [*Heiskanen and Moritz*, 1985]

$$\begin{aligned} \Delta g(r,\phi,\lambda) = \frac{\mathrm{GM}}{r^2}\sum_{n=2}^{K}(n-1)\left(\frac{a}{r}\right)^n \\ \cdot \sum_{m=0}^{n}(\Delta\bar{C}_{nm}\cos m\lambda + \Delta\bar{S}_{nm}\sin m\lambda)\bar{P}_{nm}(\sin\phi) \end{aligned} \tag{5}$$

where GM is the product of the gravitational constant and the mass of the earth, a is a scaling factor, (r, ϕ, λ) are spherical coordinates (radial distance, geocentric latitude, and longitude), n and m are degree and order of spherical harmonic, K is degree of expansion, $\bar{P}_{nm}$ is the fully normalized associated Legendre function, and $\Delta\bar{C}_{nm}$, $\Delta\bar{S}_{nm}$ are the differences between the geopotential coefficients of the earth and the geopotential coefficients of a reference ellipsoid, the latter containing only zonal coefficients. On a sphere of radius $R = R_e + z$, where R_e is the mean radius of the earth ($\approx$6371 km) and z is the altitude, the global average power of gravity anomaly to degree K is defined as

$$\begin{aligned} P(z,K) &= \frac{1}{4\pi R^2}\int_{\phi=-\pi/2}^{\pi/2}\int_{\lambda=0}^{2\pi}\Delta g^2 R^2\cos\phi\,\mathrm{d}\phi\mathrm{d}\lambda \\ &= \left(\frac{\mathrm{GM}}{R^2}\right)^2\sum_{n=2}^{K}\left(\frac{a}{R}\right)^{2n}(n-1)^2\sum_{m=0}^{n}\left(\Delta\bar{C}_{nm}^2+\Delta\bar{S}_{nm}^2\right) \\ &= \left(\frac{\mathrm{GM}}{R^2}\right)^2\sum_{n=2}^{K}\left(\frac{a}{R}\right)^{2n}(n+1)^2\sigma_n^2 \\ &= \sum_{n=2}^{K}\sigma_n^2(\Delta g) \end{aligned} \tag{6}$$

where $\sigma_n^2(\Delta g)$ happens to be the anomaly degree variance [*Moritz*, 1980]. The relation in equation (6) is obtained by applying the orthogonal relations of spherical harmonics [*Heiskanen and Moritz*, 1985, pp. 28–31] to the expansion in equation (5). The resolvable degree at an altitude z is a K such that

$$\frac{P(z,\infty)-P(z,K)}{P(z,\infty)} = \varepsilon \tag{7}$$

where ε is a small number. The resolvable wavelength at z is then [*Seeber*, 2003, p. 469]

$$\lambda_z = 111.194 \times \frac{360}{K} = \frac{40030.2}{K}\mathrm{km} \tag{8}$$

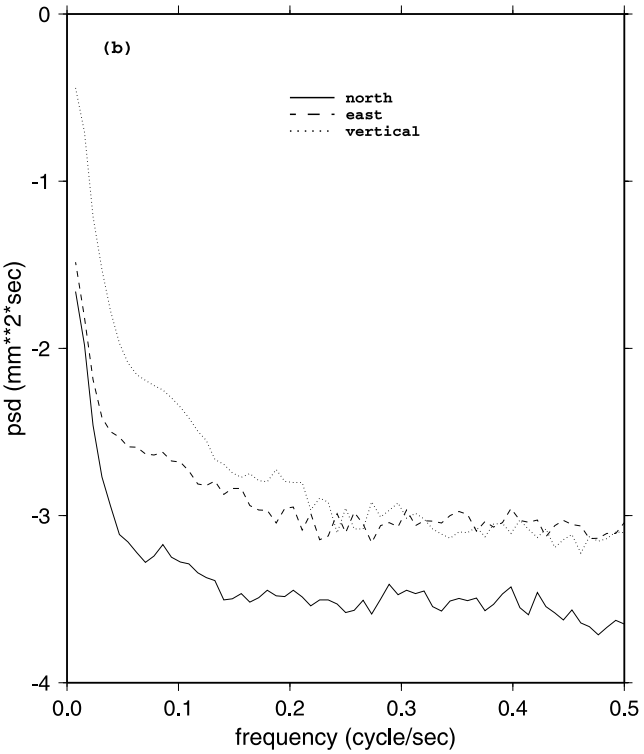

Figure 2. (continued)

[13] Note that this wavelength is due to the natural decay of gravity signal and is independent of measurement error, the latter further increasing the resolvable wavelength. We adopt $\varepsilon = 10^{-14}$, which is the limit of precision in the Institute of Electrical and Electronics Engineers (IEEE) double-precision computing environment. For the anomaly degree variances, we adopt

$$\sigma_n^2(\Delta g) = \begin{cases} \text{anomaly degree variance of GGM02C}(2 \le n \le 200) \\ \quad \text{and EGM96}(201 \le n \le 360) \\ \dfrac{A(n-1)}{(n-2)(n+24)}\sigma_0^{n+2}, \text{for } n > 361 \end{cases} \tag{9}$$

where $A = 425.28$ mgal^2 and $\sigma_0 = 0.999617$. The anomaly degree variance for $n > 361$ in equation (9) is the model 4 degree variance of *Tscherning and Rapp* [1974]. The GGM02C model provides geopotential coefficients up to a degree of 200 and is derived from Gravity Recovery and Climate Experiment's (GRACE) satellite-to-satellite tracking data and surface gravity data [*Tapley et al.*, 2004]. The EGM96 model is also derived from satellite and surface data [*Lemoine et al.*, 1998]. If the anomaly degree variances for all degrees (except $n = 2$) are based on *Tscherning and Rapp*'s [1974] model, a closed form of $P(R, \infty)$ exists. In this paper, $P(R, \infty)$ is approximated by a value obtained by setting K equivalent to a wavelength of 0.1 km. Table 2 shows the theoretical resolvable wavelengths at selected altitudes. Since the flight altitude in this airborne gravity survey is 5 km, the expected resolvable wavelength of gravity signal is about 3 km. This wavelength will be degraded by data noise.

Table 1. Averaged RMS Differences From 10 Overlapping Sessions of GPS Kinematic Solution

	North	East	Vertical
Position, m	0.073	0.208	0.293
Velocity, ms^{-1}	0.0003	0.0003	0.0013
Acceleration, mgal	23.56	26.56	104.85

Table 2. Global Averaged Resolvable Wavelength at Flight Altitude Derived From Equation (8)

Altitude, km	Resolvable Wavelength, km	Harmonic Degree
0.5	0.862	46,430
1	1.102	36,317
2	1.577	25,382
3	2.047	19,557
4	2.513	15,930
5	2.911	13,751
6	3.363	11,904
7	3.813	10,499
8	4.261	9,395
9	4.708	8,503
10	5.153	7,768

5. Data Reduction: Error Sources and Filtering

[14] The basic formula for computing along-line gravity value at the flight altitude is [*Olesen*, 2003]

$$\begin{aligned} g_z &= (f_z - f_b) - a_z + \delta g_{\text{tilt}} + g_0 + \left[2w_e \cos\phi + \frac{v_e}{(R_N + z)}\right] v_e \\ &\quad + \frac{v_n^2}{(R_M + z)} \\ &\approx (f_z - f_b) - a_z + \delta g_{\text{tilt}} + g_0 + 2w_e v_h \cos\phi \sin\alpha + \frac{v_h^2}{R_e + z} \end{aligned} \tag{10}$$

where

z: flight altitude above sea level
g_z: gravity value at z
f_z: gravity observation at z
f_b: gravity observation at the airport (base reading)
a_z: vertical acceleration of aircraft (positive to zenith)
δg_{tilt}: platform off-level correction
w_e: mean rotational velocity of the earth (7.292115×10^{-5} rad s^{-1})
ϕ: geodetic latitude
R_N, R_M: radii of curvatures along the prime vertical and the meridian [*Torge*, 2001]
R_e: mean radius of the earth
v_e, v_n: east and north velocity component
$v_h = \sqrt{v_e^2 + v_n^2}$: horizontal velocity component
α: azimuth of flight
g_0: gravity value at the parking spot (at the gravimeter level)

[15] The gravity observations f_z and f_b are derived from spring tensions, beam velocity factors, and cross-coupling

Table 3. Required Accuracy for a 1-mgal Accuracy in Airborne Gravity Value in a 1-Hz Sampling Rate for an Average Latitude of 23.5° and Velocity of 85 ms^{-1}[a]

Term	Required Accuracy
Vertical Acceleration	1 mgal, equivalent to 3.6×10^{-3} cm in VP
Horizontal Velocity	37.5 cm^{-1} for $\alpha = 0°$, 180°, equivalent to 26.7 cm in HP
	6.2 cm^{-1} for $\alpha = 90°$, equivalent to 4.4 cm in HP
	9.3 cm^{-1} for $\alpha = 270°$, equivalent to 6.6 cm in HP
Azimuth	3′ for $\alpha = 0°$, 180°, equivalent to 7.5 cm in HP
Latitude	6′57″ for $\alpha = 90°$, 270°, equivalent to 12,898 m in HP

[a]VP: vertical position, HP: horizontal position.

corrections. The platform off-level correction is derived from the kinematic accelerations of the aircraft and the accelerometer measurements [*Olesen*, 2003]. This correction will reduce the effect of platform inclination caused by the horizontal acceleration. The last two terms in equation (10) combine to form the Eötvös effect, which has been described by *Harlan* [1968]. The free-air gravity anomaly at z is computed by [*Torge*, 1989]

$$\Delta g_z = g_z - \left[\gamma_0 + \left(\frac{\partial \gamma}{\partial h}\right)h + \frac{1}{2}\left(\frac{\partial^2 \gamma}{\partial h^2}\right)h^2\right] \qquad (11)$$

where γ_0 is the normal gravity on a reference ellipsoid, h is orthometric height, and $\partial\gamma/\partial h$ and $\partial^2\gamma/\partial h^2$ are the vertical gradients of normal gravity and gravity gradient, respectively. For the gradients, we use the GRS80 reference ellipsoid so that $\partial\gamma/\partial h = -0.3087$ and $\partial^2\gamma/\partial h^2 = 2.8906 \times 10^{-7}$ (h is in meters and gravity is in milligal). The orthometric height is determined by subtracting the geoidal height of *Hwang* [1997] from the GPS-derived ellipsoidal height. The accuracy of this geoid model ranges from few centimeters in coastal plains to decimeter in high mountains (section 8). Thus the error of orthometric height is of the order of decimeter, which translates to about 0.03-mgal error in gravity anomaly. Compared with gravity value, gravity anomaly is less sensitive to variation in flight altitude [*Olesen*, 2003].

[16] The quantities z, a_z, v_e, v_n, ϕ, and α are all derived from GPS positioning results. Their errors will contribute to the error of gravity value. Given a required accuracy of gravity value (g_z), it will be useful to know the accuracy requirements of these quantities. Ignoring changes in gravimeter reading, airport gravity value, and off-level correction, the differential change of gravity value is

$$dg_z = -da_z + \left(2w_e \cos\phi \sin\alpha + \frac{2v_h}{R_e + z}\right)dv_h + 2w_e v_h \cos\phi \cos\alpha d\alpha - 2w_e v_h \sin\phi \sin\alpha d\phi \qquad (12)$$

[17] This relation can be used for computing accuracy requirements. Assuming dg_z = 1 mgal, Table 3 lists the required accuracies of vertical acceleration, horizontal velocity, azimuth, and latitude of the aircraft for a speed of 306 km/hour and a mean latitude of 23.5° and a 1-Hz sampling rate. For each term in Table 3, whenever possible, the equivalent accuracies of positioning are also computed using the approximations in equation (4) (the long-wavelength positioning error is not included). According to Table 3, for a 1-mgal accuracy of a_z, the equivalent accuracies of horizontal velocity and position are too demanding to be achieved by GPS today. For other terms, the required accuracies of horizontal velocity and position can be achieved by GPS, as shown in Table 1.

Table 4. Average RMS Differences of Vertical Acceleration and Horizontal Velocity From 10 Overlapping Sessions of Lines as a Function of Filter Width

Filter Width, s	Vertical Acceleration, mgal	Horizontal Velocity, ms^{-1}
0	104.85	0.000396
60	1.09	0.000025
90	0.58	0.000020
120	0.37	0.000020
180	0.19	0.000018
240	0.12	0.000017
300	0.09	0.000017
400	0.07	0.000016

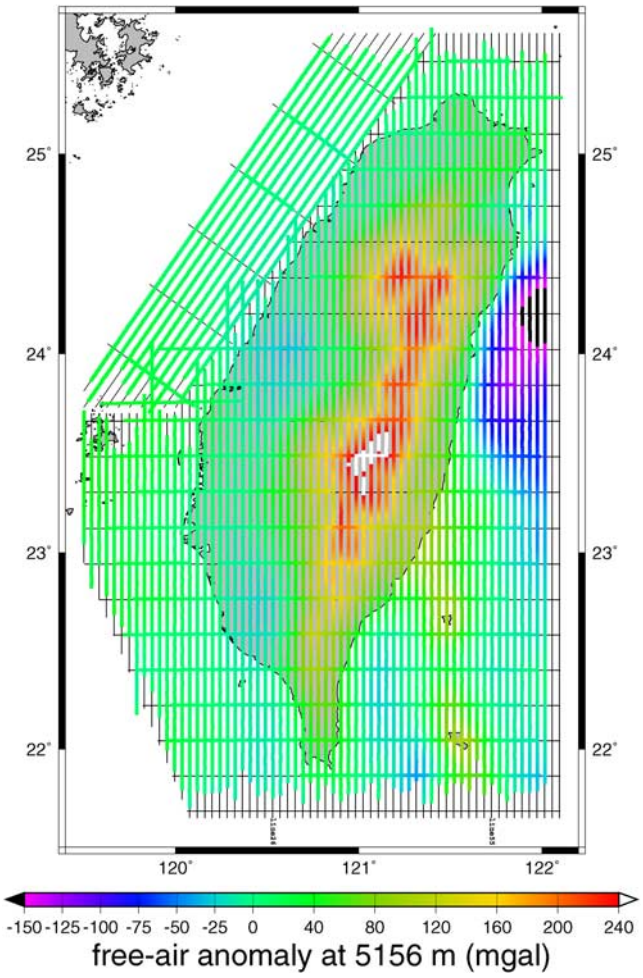

Figure 3. Gravity anomalies at the flight altitude. Repeat flights are made at lines 26 and 55.

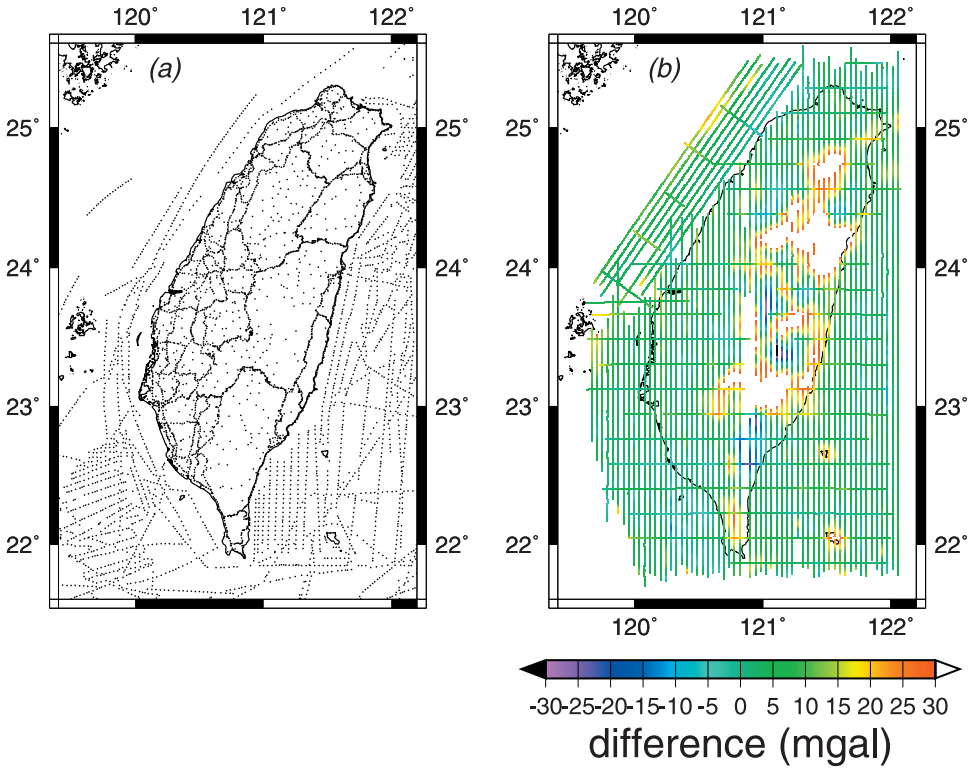

Figure 4. (a) Distribution of surface gravity anomalies; (b) differences between surface (upward continued) and raw airborne gravity anomalies.

[18] One solution to the problem of a_z and other data noises is filtering. An ideal filter will be one that properly removes data noises while preserving maximum gravity information. Table 4 shows the RMS differences of GPS-derived vertical acceleration as a function of Gaussian filter width at the overlapping sessions of section 3.2. The Gaussian filter here is exactly the same as that defined in the Generic Mapping Tools software [*Wessel and Smith*, 1999]. The Gaussian filter used in this paper is described by *Hwang et al.* [2006] and employs an iterative filtering to down-weight outliers. The filter width is a window of convolution in the filtering, and it is equal to resolvable wavelength. Other options of filter for airborne gravimetry are discussed by, e.g., *Hammada* [1996], *Childers et al.* [1999], and *Olesen* [2003]. The second-order Butterworth filter used by *Olesen* [2003] has also been tested in this paper and it yields the same results in most occasions. Table 4 shows that RMS difference decreases with increasing filter width. According to Table 4 (filter width = 0), the long-wavelength errors in GPS positioning (Figure 2a) result in an average error of order of 0.0001 ms^{-1}, which introduces an error much smaller than 1 mgal in gravity anomaly (Table 3). Also, a 1-mgal accuracy of vertical acceleration can be achieved with a filter width of about 60 s. The corresponding spatial resolution is coarser than the theoretical one discussed in section 4. However, in the actual flight, other factors than a_z will introduce errors to gravity measurements [*Olesen*, 2003]. After some tests, it is decided to adopt a filter width of 150 s for the Gaussian filter. This corresponds to a 6-km spatial resolution (half wavelength). Figure 3 shows the filtered along-line gravity anomalies at the flight altitude obtained in this work.

6. Accuracy Assessment of Airborne Gravity Anomaly

6.1. Comparison with Surface Gravity Data

[19] Our accuracy assessment of gravity anomaly begins with comparing the airborne and existing surface gravity anomalies (Figure 4a). The land gravity data were collected by *Yen et al.* [1990] in Taiwan's triangulation networks and by MOI in the first-order leveling network. Their accuracies vary from sub-milligal to milligal. The shipborne gravity data were supplied by *Hsu et al.* [1998], and the data noises are at the mgal level. For comparison, the long-wavelength gravity anomalies of the combined GGM02C and EGM06 model are first removed from the surface gravity anomalies. The residual gravity anomalies were gridded and then upward continued to the flight altitude using

$$\mathbf{G}_z(u,v) = e^{-2\pi z\sqrt{u^2+v^2}}\mathbf{G}_0(u,v) \tag{13}$$

where u and v are spatial frequencies and $\mathbf{G}_0$ and $\mathbf{G}_z$ are the Fourier transforms of gravity anomalies at sea level and at the flight altitude. The long-wavelength gravity anomalies of the combined GGM02C and EGM06 model at z were then restored.

[20] Figure 4b shows the differences between the upward continued and the airborne gravity anomalies. Most of the large differences occur in high mountains and few occur

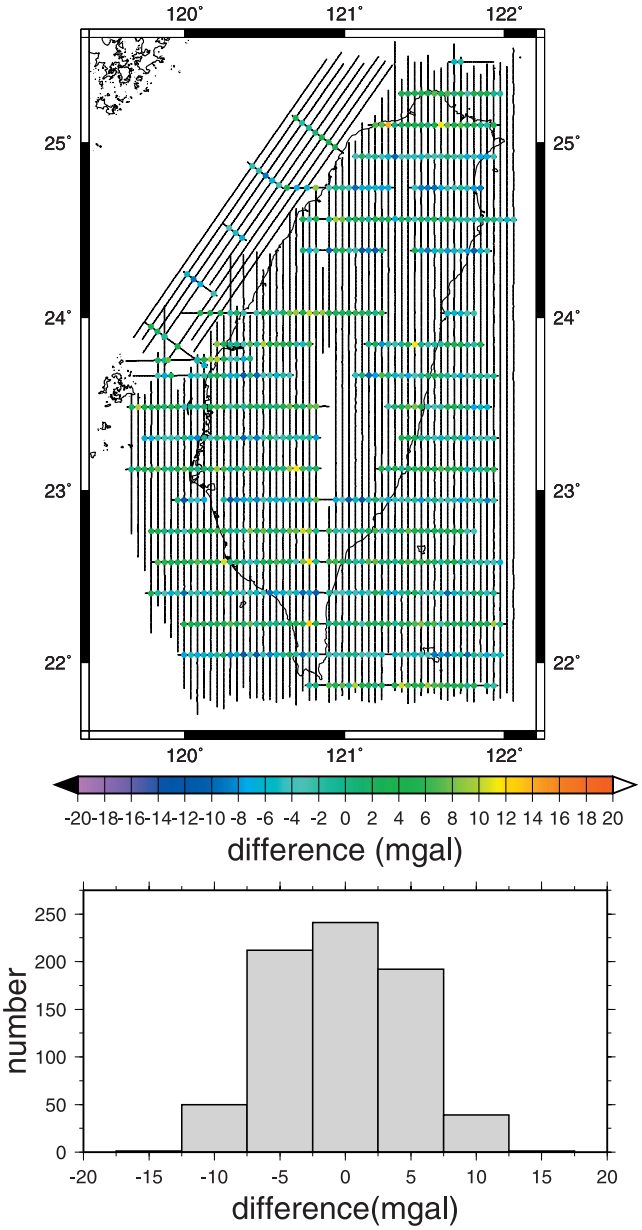

Figure 5. Distribution and histogram of crossover differences of gravity anomalies.

over the waters east of Taiwan. These large differences come from the following sources.

[21] (1) Errors in airborne gravity measurements; for example, the scattering large differences along four north-south lines east of Taiwan.

[22] (2) Data density and quality of surface gravity anomalies. For example, relatively large differences occur at the immediate vicinity of all coasts, the Central Range and the waters northwest of Taiwan, because here the surface data densities are relatively low.

[23] (3) Large gravity gradients at areas of rough gravity fields.

[24] (4) Possible computation error of upward continuation. It is noticed that the gravity fields over the Central Range (low-surface data density) and over the ocean trench east of Taiwan (high-surface data density) are equally rough, but large differences are found only over the Central Range. This indicates that the differences in Figure 4b are largely dominated by surface data density rather than errors in airborne gravity measurements. However, Figure 4b does indicate that there are still many suspicious airborne measurements, which were removed manually for subsequent applications.

6.2. Crossover Analysis

[25] A crossover difference is the difference of the two gravity values at the intersection of two survey lines. In most cases, the exact crossover point of two lines does not exist, thus linear interpolation must be used to find the crossover location. Figure 5 shows the crossover differences (total 736) and a histogram of these values. Due to bad GPS data and turbulences, some crossover differences are excessively large and a crossover difference larger than 15 mgal is considered an outlier and is not used for the subsequent analyses. The distribution of crossover differences approximately follows the normal distribution, suggesting that these crossover differences are largely due to random noises. Similar to the pattern of difference between upward-continued and airborne gravity anomalies (Figure 4b), large crossover differences occur in high mountains and along lines with bad data. Crossover difference is partly caused by interpolation error, especially over areas with a rough gravity field. According to equation (10) and Table 3, for the Eötvös effect, the required accuracy of velocity (about 6 to 9 cm^{-1}) in the west-east direction is higher than that in the north-south direction (about 37 cm^{-1}). Under the same order of velocity accuracy, the west-east lines are likely to contain larger errors in gravity and in turn cause larger crossover differences, compared with the north-south lines. Therefore some of the large crossover differences may be due to poor horizontal velocity accuracy along west-east lines.

[26] In order to reduce possible systematic errors, we performed a crossover adjustment using the weighted constraint method developed by *Hwang et al.* [2006]. In the adjustment, gravity anomalies on a survey line are assumed to be corrupted by a bias. Since the reported drift of the LCR air-sea gravimeter is less than 3 mgal/month and each session of flight lasts only for about 4 hours, the effect of gravimeter drift is not modeled. In order to eliminate the rank defect in the adjustment, at least one survey line must be held fixed. We find that gravity values along survey lines 18 and 54 agree very well with upward-continued surface gravity anomalies (section 6.1), so they were held fixed in the adjustment. Also, survey lines with less than two crossover differences are not adjusted. Table 5 shows the statistics of the crossover differences before and after the adjustment. The adjustment reduced the crossover differences. The adjustment also reduces the discrepancy between airborne and surface (upward continued) gravity anomalies from 12.4 (Figure 4b) to 11.8 mgal. Figure 6 shows the estimated biases of gravity anomalies along all survey lines.

Table 5. Statistics of Crossover Difference of Airborne Gravity Anomaly (mgal)

Case	Max	Min	Mean	RMS
Before Adjustment	13.97	−13.33	−0.24	4.92
After Adjustment	10.07	−9.17	0.00	2.88

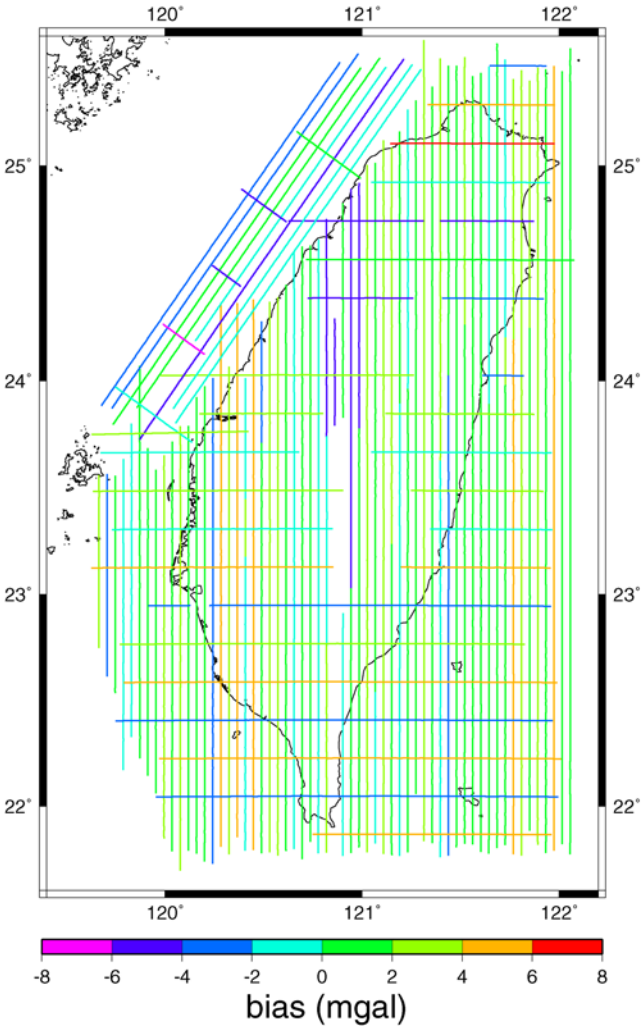

Figure 6. Estimated biases of survey lines from the crossover adjustment.

The biases are about few milligal, and there is no specific pattern in the distribution of the biases. A bias along a survey line could be caused by, for example, improper base readings, "tare" in a sudden turbulence, and problems in GPS results. Assuming that the RMS difference after the adjustment is solely due to random noises, it is estimated that the averaged standard error of airborne gravity anomalies collected in this work is about $2.88/\sqrt{2} \approx 2$ mgal at a spatial resolution of 6 km.

6.3. Repeatability Analysis

[27] Repeatability quantifies the basic precision of a measurement system. In order to determine the airborne measurement repeatability and to identify the factors governing the repeatability, parts of lines 26 and 55 (Figure 3) were flown twice. Line 26 is a north-south line over the southwestern coastal plain, and line 55 is also a north-south line over the Pacific Ocean east of Taiwan. The repeatability standard deviation is chosen as an index of measurement precision and is calculated as the standard deviation of the differences at all repeat measurement points. Figure 7 shows the standard deviations as a function of filter width. For both lines, the standard deviation decreases with increasing filter width, but becomes flat beyond a certain filter width. At filter widths smaller than 75 s, the standard deviations of line 26 are higher than those of line 55 (Figure 7). Beyond 75 s, the standard deviation of line 55 overtakes that of line 26, and eventually, it is about twice as large as that of line 26.

[28] Under a favorable condition, such as that associated with line 26, the airborne gravity measurement system delivers the same level of accuracy of gravity data in repeat flights. However, this favorable condition does not happen to the repeat flights of line 55, leading to the larger repeatability standard deviation (at filter widths > 75 s). The dominating factor is the GPS positioning. According to *Forsberg et al.* [2003], spurious GPS results can easily cause error in gravity value up to tens of milligal. In the first flight of line 55, some of the estimated aircraft coordinates appear to be in error due to changes in the number of visible GPS satellite and disturbances of unknown sources. The iterative Gaussian filter cannot remove these errors. Also, we found that the mean difference between the surface gravity values and those from first flight of line 55 is about 10 mgal, while for line 26, the mean difference between repeat flights is only 1 mgal. Regarding the higher standard deviations of line 26 than line 55 at filter widths smaller than 75 s, one possible explanation is that the long-wavelength positioning errors in one or two of the flights of line 26 at lower frequencies are larger than the counterparts of line 55.

[29] As shown in Figure 7, at the filter width of 150 s, the repeatability standard deviation of line 26 is about 3 mgal and it does not decrease significantly as the filter width increases. Since increasing the filter width will remove detailed gravity information, it seems that a filter width of 150 s is a compromise between noise reduction and gravity signal preservation.

7. Downward Continuation: Fourier Transform vs. Least-Squares Collocation

[30] Downward continuation of airborne gravity anomalies to sea level is needed for such applications as geoid modeling, plate tectonic investigation, and orthometric correction. Techniques of downward continuation are abundant in the literature. It is not the intent of this paper to

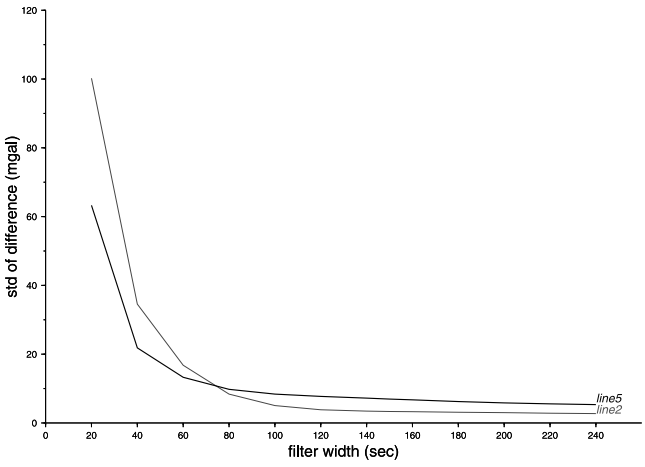

Figure 7. Standard deviation of differences of gravity anomalies from two repeat flights.

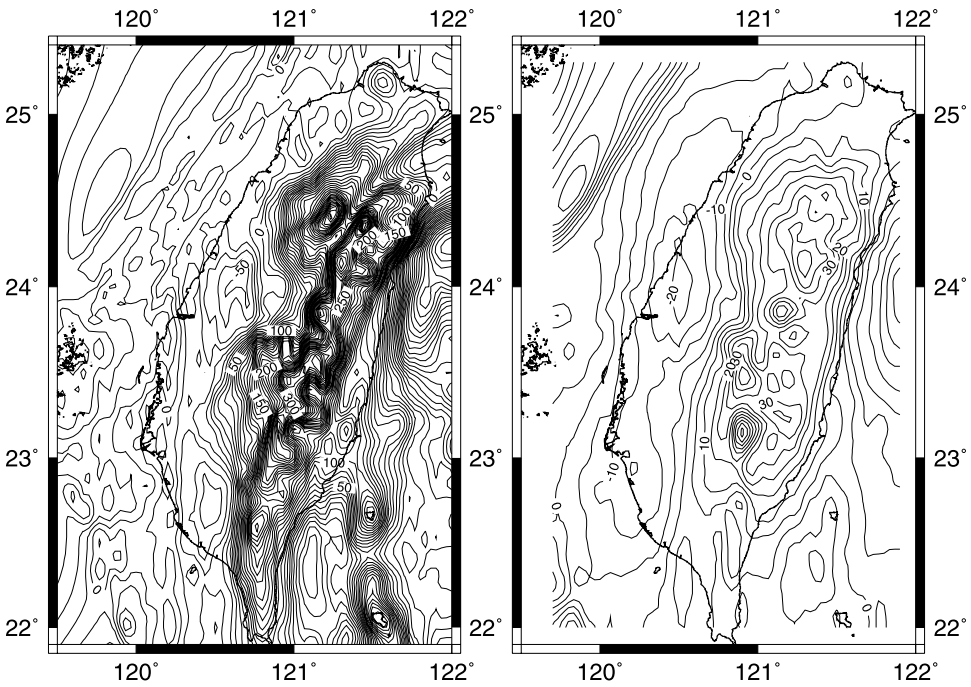

Figure 8. Downward-continued gravity anomalies (at sea level) by least-squares collocation (left) and the differences between the results from least-squares collocation and from Fourier transform (15-km filter). Unit is mgal.

investigate all possible methods. Here we experimented with two methods of downward continuation: Fourier transform and least-squares collocation. The remove-restore procedure is used in both methods, with the combined GGM02C and EGM96 model being the long-wavelength gravity field. In the Fourier transform approach, the relation in equation (13) is reversed and a filter is introduced so that [cf. *Buttkus*, 2000]

$$\mathbf{G}_0(u,v) = e^{2\pi z\sqrt{u^2+v^2}}\mathbf{W}(u,v)\mathbf{G}_z(u,v) \tag{14}$$

where $\mathbf{W}$ is a frequency-domain filter. As an alternative to the frequency-domain filtering, one can set $\mathbf{W} = 1$ in equation (14) and apply a space-domain filter to the unfiltered, downward-continued gravity anomalies. In this paper, a space-domain Gaussian filter has been used in the Fourier transform approach.

[31] Downward continuation using least-squares collocation can be expressed as [cf. *Moritz*, 1980]

$$\Delta\mathbf{g}_0 = \mathbf{C}_{0z}\left(\mathbf{C}_g + \mathbf{C}_n\right)^{-1}\Delta\mathbf{g}_z \tag{15}$$

where $\Delta\mathbf{g}_0$, $\Delta\mathbf{g}_z$ are vectors containing gravity anomalies at sea level and at z, $\mathbf{C}_{0z}$ is the cross-covariance matrix between gravity anomalies at sea level and at z, and $\mathbf{C}_g$ and $\mathbf{C}_n$ are the covariance matrices of the signal and noise parts of $\Delta\mathbf{g}_z$. $\mathbf{C}_n$ is a diagonal matrix, and its diagonal elements are the inverses of data error variances. $\mathbf{C}_n$ works as a filter and a stabilizer in the least-squares collocation downward continuation, and the degree of filtering increases with the error variance. In this paper, we use an error variance of 9 mgal^2 as obtained from the crossover and repeatability analyses (section 5). We use the model 4 degree variance of *Tscherning and Rapp* [1974] in equation (9) to construct matrices $\mathbf{C}_{0z}$ and $\mathbf{C}_g$.

[32] As expected, Fourier transform without filtering produces gravity anomalies containing large noise and edge effect. As a compromise between noise reduction and optimal spatial resolution, the final result with the Fourier transform is obtained by filtering the downward-continued gravity anomalies by the Gaussian filter with a filter width of 15 km. Figure 8 shows the downward-continued gravity anomalies using least-squares collocation and the differences in gravity anomaly by using the least-squares collocation and Fourier transform methods. The differences are correlated with the roughness of gravity field, and generally, the difference increases with the degree of gravity roughness. Table 6 shows the statistics of the differences between the downward-continued and the surface gravity anomalies (Figure 4a). Because of the edge effect in Fourier transform, gravity anomalies at the 0.2° borders are excluded in the statistics. The comparisons were made over regions of different elevations. The overall RMS differences from these two methods differ only marginally (0.8 mgal). However, least-squares collocation yields a smaller RMS difference than Fourier transform at elevations less than 2000 m. In particular, the RMS difference from least-squares collocation is 2.2 mgal smaller than that from Fourier transform. According to these comparisons, least-squares collocation is recommended as the method for downward continuation.

8. Geoid Models From Airborne and Other Gravity Data

[33] One application of airborne gravimetry is geoid modeling. A best geoid model will be one that is derived

Table 6. Statistics of Differences (in mgal) Between Downward-Continued and Surface Gravity Anomalies

Area for Statistics	Min	Max	Mean	RMS
All	−146.9[a], −158.9[b]	124.7[a], 102.1[b]	−2.8[a], −5.1[b]	19.5[a], 20.3[b]
Elevation < 2000 m	−146.9, −158.9	124.7, 102.1	−3.3, −4.0	18.5, 18.4
Elevation < 1500 m	−146.9, −158.9	124.7, 102.1	−4.2, −3.7	16.6, 16.5
Elevation < 1000 m	−146.9, −158.9	94.0, 77.0	−4.9, −3.2	14.2, 13.5
Elevation < 500 m	−113.7, −120.6	80.4, 54.2	−5.6, −2.5	11.7, 9.9
Sea Only	−44.0, −41.9	26.1, 25.6	−5.0, −1.9	9.9, 7.4

[a]Fourier transform.
[b]Least-squares collocation.

from all possible data sources in an optimal way of data combination. For the geoid modeling in this paper, the data available are the airborne and surface gravity anomalies and the KMS02 altimeter-derived gravity anomalies [*Andersen et al.*, 1999]. For cross-validation, we experimented with two methods of geoid modeling: Fourier transform and least-squares collocation-based methods. In both methods, a terrain-assisted remove-restore procedure was used. First, the residual terrain model (RTM) gravity effect [*Forsberg*, 1984] and the long-wavelength gravity field from the combined GGM02C and EGM96 model were removed. A 3″ × 3″ digital elevation model of Taiwan was used for the RTM effects. The residual geoidal heights were then computed from residual gravity anomalies and added to the RTM and the GGM02C-EGM96-implied geoidal heights to produce the final model.

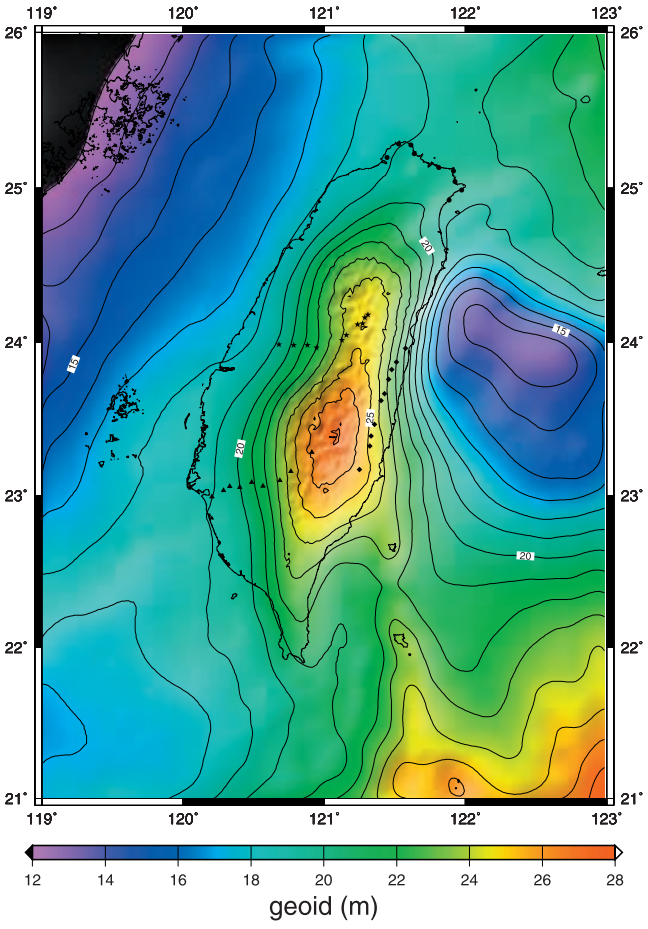

Figure 9. The geoid model of Taiwan from the KMS method. Circles represent benchmarks along the north leveling route, stars represent the center route, triangles represent the south route, and diamonds represent the east route.

[34] The difference between the two methods lies in the way the airborne gravity anomalies are used, and in the way, the residual geoidal heights are computed. In the first method, named the KMS method, the residual airborne gravity anomalies were first downward-continued to sea level and then combined with other gravity data to form a grid of residual gravity anomaly. The residual gravity grid was then transformed to a residual geoid grid by Stokes' integral, which was implemented by a multiband Fourier transform technique [*Forsberg and Sideris*, 1993]. Figure 9 shows the KMS geoid model. In the second method, named the NCTU method, the residual airborne and residual surface gravity anomalies were directly used to compute residual geoidal heights using least-squares collocation. Thus, least-squares collocation combines downward continuation and geoid computation in one step. The formula of the least-squares collocation used is similar to equation (15). Again, the anomaly degree variance model of *Tscherning and Rapp* [1974] was used in constructing the needed covariance matrices. The detail of geoid modeling by least-squares collocation in this paper is described by *Hwang* [1997].

[35] The KMS and NCTU geoid models were evaluated using the "observed" geoidal heights along four first-order leveling routes (Figure 9). An "observed" geoidal height is the difference between the GPS-derived ellipsoidal height (from a 24-hour observation and at centimeter-level accuracy) and the precision leveling-derived orthometric height (at millimeter-level accuracy). For the precision leveling result, rigorous orthometric corrections have been applied [*Hwang and Hsiao*, 2003]. The geoid variation is smooth along the north route (range: less than 1 m), mild (range: about 3 m) along the east route, and rough along the center and south routes (range: more than 8 m). Table 7 shows the standard deviations of differences between the "observed" and the modeled geoidal heights at the four leveling routes. In Table 7, *Hwang*'s [1997] geoid model is based on surface

Table 7. Standard Deviations of Differences (in m) Between Observed and Modeled Geoidal Heights at Four Leveling Routes

Geoid Model	North Route	Center Route	South Route	East Route
KMS	0.059	0.187	0.080	0.022
NCTU	0.002	0.116	0.190	0.055
Hwang [1997]	0.080	0.258	0.222	0.140

gravity data only (Figure 4a). The standard deviations range from centimeter in coastal plains to decimeter in high mountains. The major improvement of current geoid models over *Hwang*'s [1997] model is in high mountains (the center and south routes) where current land gravity data are sparsely distributed and geoid variation is large.

[36] The gravity data used above have been treated as if they contained full signal components, although the truth is that the airborne, shipborne, and altimeter-derived gravity anomalies have been filtered in different ways. Therefore the airborne gravity will contribute to the local gravity field only at certain wave bands. It will require a more sophisticated technique of geoid modeling than least-squares collocation if gravity data of different wave bands are to be combined for a best geoid model. One such technique is based on the concept of multiresolution [e.g., *Schwarz and Li*, 1997]. Alternative methods of geoid modeling using airborne and surface data are presented by, e.g., *Bayoud and Sideris* [2003], *Novak et al.* [2003], and *Alberts and Klees* [2004]. These methods will be a subject of future study.

9. Bouguer Anomaly

[37] As a geophysical product, Bouguer anomalies were computed from the airborne gravity data. We employed a pointwise algorithm for the computation. As shown in Figure 10, the perturbing potential due to the mass between the sea level and the surface is

$$V = G\int_x\int_y\int_{z=0}^{h}\frac{\rho \mathrm{d}x\mathrm{d}y\mathrm{d}z}{\sqrt{(x-x_\mathrm{p})^2+(y-y_\mathrm{p})^2+(z-s)^2}} \qquad (16)$$

where G is defined in equation (5) and ρ is the density of the terrain. At point P of the flight altitude, the gravity effect due to the terrain is

$$A_\mathrm{T} = -\left(\frac{\partial V}{\partial s}\right)|_{s=h_\mathrm{p}} = G\int_x\int_y \rho f(x,y)\mathrm{d}x\mathrm{d}y \qquad (17)$$

where

$$f(x,y) = \frac{1}{\left[(x-x_\mathrm{P})^2+(y-y_\mathrm{P})^2+(h-h_\mathrm{p})^2\right]^{1/2}} - \frac{1}{\left[(x-x_\mathrm{P})^2+(y-y_\mathrm{P})^2+h_\mathrm{p}^2\right]^{1/2}} \qquad (18)$$

[38] Thus the Bouguer anomaly at the flight altitude is

$$B_\mathrm{a} = \Delta g - A_\mathrm{T} \qquad (19)$$

where Δg is free-air gravity anomaly at the flight altitude. In equation (17), the density is set to 2.67 g cm^{-3} at land and 1.64 g cm^{-3} at sea. The elevation h in equation (18) is positive at land and negative at sea. By this method, Bouguer anomalies at land and sea can be computed.

[39] A Gaussian quadrature method, which is similar to that used for rigorous terrain correction [*Hwang et al.*, 2003], is used to implement equation (17). Using a planar approximation, with X_1 (west), X_2 (east), Y_1 (south), and Y_2 (north) being boundaries, equation (17) is implemented as

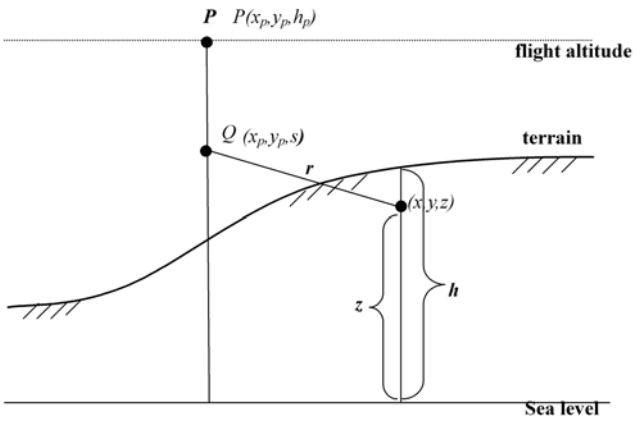

Figure 10. Geometry showing terrain effect at the flight altitude.

$$A_\mathrm{T} = G\int_{X_1}^{X_2}\int_{Y_1}^{Y_2}\rho f(x,y)\mathrm{d}x\mathrm{d}y \approx G\sum_{j=1}^{M} w_j^y c(y_j) \qquad (20)$$

with

$$c(y) = \int_{X_1}^{X_2}\rho f(x,y)\mathrm{d}x \approx \sum_{i=1}^{N} w_i^x \rho f(x_i,y) \qquad (21)$$

where w_i^x and w_j^y are weighting coefficients, x_i and y_j are nodal coordinates corresponding to the coefficients, and M and N are number of nodes between X_1 and X_2, and between Y_1 and Y_2, respectively [cf. *Press et al.*,1989]. The computation using equation (20) is divided into the inner zone and the outer zone. For the inner zone and outer zones, a $9'' \times 9''$ and a $90'' \times 90''$ elevation grid are used. The adopted radii of the inner and outer zones are 20 and 200 km, respectively. Furthermore, Bouguer anomaly at sea level is computed using the following steps:

[40] Step 1: Interpolate the orthometric height at a surface point corresponding to the point of airborne gravity measurement using the $9'' \times 9''$ elevation grid. At sea, the orthometric height is zero, so no interpolation is needed.

[41] Step 2: Compute the terrain effect using the same algorithm as that for Bouguer anomaly at the flight altitude (by setting s to the orthometric height in equation (17)).

[42] Step 3: Subtract the terrain effect from Step 2 from the downward-continued gravity anomalies (by least-squares collocation) to obtain Bouguer anomaly at sea level.

[43] Figure 11 shows the Bouguer anomalies at the flight altitude and at sea level. On the basis of a visual inspection, the Bouguer anomalies from this work agree well with those from *Yen et al.* [1998] in pattern and magnitude. The Bouguer anomalies of Yen et al. were derived from land gravity measurements and a coarser elevation grid by a different numerical technique than the Gauss quadrature. In eastern Taiwan, Bouguer anomalies are mostly positive and are typical over plate collision zones (in this case: the Philippine Sea Plate and the Eurasian Plate) that contain

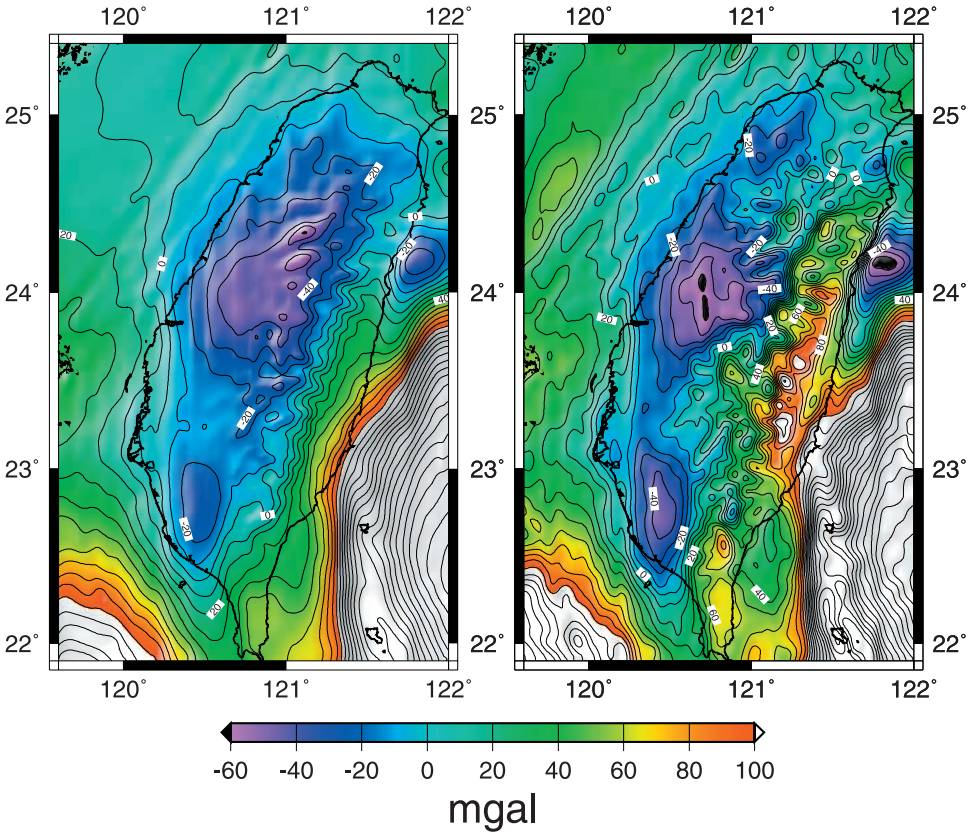

Figure 11. Bouguer anomalies at the flight altitude (left) and sea level.

rocks of higher densities. Toward the Heng-Chun Peninsula, the higher anomalies are caused by the oceanic crust underneath. A high exists in the northern tip of Taiwan because of the presence of the Tatun and Chilung volcanoes. The positive anomalies stretching from the Peng-Hu Island (at about 23.5°N, 119.5°E) in the Taiwan Strait to western Taiwan are associated with the Peikang Basement High. Over the oceanic plates east of Taiwan and over the South China Sea, the anomalies are mostly positive, except at a circular spot centered at about 24.2°N and 121.8°E, where thick sediments are deposited over the Ho-Ping Ocean Basin. In the western and northeastern coastal plains and the waters northwest of Taiwan, the anomalies are mostly negative and are due to sedimentations here. A distinct, circular low centered at 24°N and 120.8°E is the result of the westward thrust of Paleogence rocks over the Neogene units [*Yen et al.*, 1998]. A comprehensive geophysical investigation of Bouguer anomalies derived from this work is left to interested readers.

10. Conclusions

[44] This paper presents the result of a recent airborne gravity survey of Taiwan. An assessment of GPS kinematic positioning results shows that the trajectories of the aircraft are determined to a decimeter-level accuracy. Some of the positioning errors are of long-period nature, which introduce lesser effects on velocity and acceleration upon differentiation. A procedure, with formulae based on the global average power of gravity anomaly, is presented and can be used to predict a theoretical resolvable wavelength of airborne gravimetry at a given flight altitude. The analyses of crossover differences and repeat airborne measurements suggest that the overall accuracy of the airborne gravity anomalies is about 2 to 3 mgal at a spatial resolution of 6 km (half wavelength). The airborne gravity anomalies agree well with exiting surface gravity data, except in high mountains and locations of sparse surface data.

[45] We employed the Fourier transform and least-squares collocation methods to downward-continue airborne gravity anomalies to sea level. In general, least-squares collocation outperforms Fourier transform based on comparison with surface data. Two geoid models were computed using airborne and surface gravity data. Evaluations of these models at four first-order leveling routes suggest that the model accuracy ranges from centimeter in coastal plains to decimeter in high mountains. We also computed Bouguer anomalies by a rigorous numerical approach. Geophysical investigations of the many interesting tectonic features in the Bouguer anomaly are needed.

[46] Here we point out some subjects of future investigations. The iterative Gaussian filter used in this paper yields airborne gravity anomalies at a spatial resolution of 6 km. This resolution may be improved by employing an optimal filter that can minimize noise while maximizing resolution. An improved result of kinematic positioning of aircraft is also possible by a careful preprocessing of GPS data, focusing on the sources of long-wavelength errors. A balance between noise reduction and resolution preservation in downward continuation is an issue worth more investigations. Finally, the current geoid models can be improved by using a method that will optimally combine band-limited

gravity data (airborne, shipborne, and altimeter-derived) and full-banded land gravity data.

[47] **Acknowledgments.** We are grateful to the pilots and navigators of King-Air Beechcraft-200 for their help. We thank R.E. Bell, P. Elosegui, and an anonymous reviewer for their constructive comments. This study is funded by the Ministry of the Interior and National Science Council of Taiwan (project 93-2211-E-009-006).

References

Alberts, B., and R. Klees (2004), A comparison of methods for the inversion of airborne gravity data, *J. Geod.*, *78*, 55–65.

Andersen, O. B., P. Knudsen, S. Kenyon, and R. Trimmer (1999), Recent improvement in the KMS global marine gravity field, *Boll Geofis. Teor. Ed Appl*, *40*, 369–377.

Angelier, J., H. T. Chu, and J. C. Lee (1997), Shear concentration in a collision zone: Kinematics of the active Chihshang Fault, Longitudinal Valley, eastern Taiwan, *Tectonophysics*, *274*, 117–144.

Bayoud, F. A., and M. G. Sideris (2003), Two different methodologies for geoid determination from surface and airborne gravity data, *Geophys. J. Int.*, *155*, 914–922.

Bell, R. E., V. A. Childers, R. A. Arko, D. D. Blankeship, and J. M. Brozena (1999), Airborne gravity and precise positioning for geologic applications, *J. Geophys. Res.*, *104*, 15,281–15,292.

Beutler, G., et al. (2004), *Bernese GPS software version 5.0 Draft*, Astronomical Institute, University of Bern, Bern, Switzerland.

Buttkus, B. (2000), *Spectral Analysis and Filter Theory in Applied Geophysics*, Springer, New York.

Childers, V. A., R. E. Bell, and J. M. Brozena (1999), Airborne gravimetry: An investigation of filtering, *Geophysics*, *64*(4), 61–69.

Childers, V. A., A. D. C. McAdoo, J. M. Brozena, and S. W. Laxon (2001), New gravity data in the Arctic Ocean: Comparison of airborne and ERS gravity, *J. Geophys. Res.*, *106*, 8871–8886.

Forsberg, R. (1984), A study of terrain reductions, density anomalies and geophysical inversion methods in gravity field modeling, in *Rep. 355*, Dept. of Geod. Sci. and Surv., Ohio State Univ., Columbus.

Forsberg, R., and M. G. Sideris (1993), Geoid computations by the multiband spherical FFT approach, *Manuscr. Geod.*, *18*, 82–90.

Forsberg, R., and D. Solheim (2000), Geoid of the Nordic/Baltic region from surface/airborne gravimetry and GPS drapping, IAG International Symposium on Gravity, Geoid, and Geodynamics 2000, Banff, Canada, 31 July–4 August.

Forsberg, R., K. Keller, S. M. Hvidegaard, and A. Olesen (2003), European airborne gravity and lidar survey in the Arctic Ocean, *ESAG-2002 final report*, Copenhagen, Denmark.

Hammada, Y. (1996), A comparison of filtering techniques for airborne gravimetry, in *UCGE Rep. No. 20089*, Dept. of Geomatics Engineering, The University of Calgary, Calgary, Alberta, Canada.

Harlan, R. B. (1968), Eötvös corrections for airborne gravimetry, *J. Geophys. Res.*, *3*, 4675–4679.

Heiskanen, W. A., and H. Moritz (1985), *Physical Geodesy*, reprint, Tech University Graz, Austria.

Hsu, S. K., C. S. Liu, C. T. Shyu, S. Y. Liu, J. C. Sibuet, S. Lallemand, C. Wang, and D. Reed (1998), New gravity and magnetic anomaly maps in the Taiwan-Luzon region and their preliminary interpretation, *Terr. Atmos. Ocean. Sci.*, *9*, 509–532.

Hwang, C. (1997), Analysis of some systematic errors affecting altimeter-derived sea surface gradient with application to geoid determination over Taiwan, *J. Geod.*, *71*, 113–130.

Hwang, C., and Y. S. Hsiao (2003), Orthometric correction from leveling, gravity, density and elevation data: A case study in Taiwan, *J. Geod.*, *77*, 279–291.

Hwang, C., and M. J. Lin (1998), Fast integration of low orbiter's trajectory perturbed by earth's nonsphericity, *J. Geod.*, *72*, 578–585.

Hwang, C., C. G. Wang, and Y. S. Hsiao (2003), Terrain correction computation using Gaussian quadrature: Effect of innermost zone, *Comput. Geosci.*, *29*(13), 1259–1268.

Hwang, C., Y. S. Hsiao, and H. C. Shih (2006), Data reduction in scalar airborne gravimetry: Theory, software and case study in Taiwan, *Comput. Geosci.*, *32*(10), 1573–1584, doi:10.1016/j.cageo.2006.02.015, in press.

Kennedy, S. L., A. M. Bruton, and K. P. Schwarz (2002), Improving DGPS accelerations for airborne gravimetry: GPS carrier phase accelerations revisited, in *Vistas for Geodesy in the New Millennium*, *Int. Ass. Geod. Sym.*, vol. 125, edited by J. Adám and K.-P. Schwarz, pp. 211–216, Springer, New York.

Kouba, J. (2003), *A Guide to Using International GPS Service (IGS) Products, IGS Publications*, IGS Central Bureau, http://igscb.jpl.nasa.gov/overview/pubs.html.

Lemoine, F. G., et al. (1998), The development of joint NASA GSFC and the National Imagery and Mapping Agency (NIMA) Geopotential Model EGM96, in *Rep. NASA/TP-1998-20686*, 575 pp., National Aeronautics and Space Administration, Greenbelt, MD.

L&R Air-Sea Gravity System II (2003), *Model "S" Air-Sea Dynamic Gravity Meter System, LaCoste & Romberg Instruction Manual*, LaCoste & Romberg LLC, Austin, Texas.

Moritz, H. (1980), *Advanced Physical Geodesy*, Herbert Wichmann Verlag, Karlsruhe.

Novak, P., M. Kern, K. P. Schwarz, M. G. Sideris, B. Heck, S. Ferguson, Y. Hammada, and M. Wei (2003), On geoid determination from airborne gravity, *J. Geod.*, *76*(9–10), 510–522.

Olesen, A. V. (2003), Improved airborne scalar gravimetry for regional gravity filed mapping and geoid determination, in *Tech. Rep. No. 24*, National Survey and Cadastre-Denmark, Copenhagen, Denmark.

Olesen, A. V., R. Forsberg, K. Keller, and A. Gidskehaug (2000), Airborne gravity survey of Lincoln Sea and Wandel Sea, North Greenland, *Phys. Chem. Earth, Part A Solid Earth Geod.*, *25*, 25–29.

Press, W. H., B. P. Flannery, S. A. Teukolsky, and W. T. Vetterling (1989), *Numerical Recipes*. Cambridge Univ. Press, New York.

Seeber, G. (2003), *Satellite Geodesy*, 2nd ed., Walter de Gruyter, New York.

Schwarz, K. P., and Z. Li (1997), Introduction to airborne gravimetry and its boundary value problems, in *Geodetic Boundary Value Problems in View of the One Centimeter Geoid, Lecture Notes in Earth Sciences*, vol. 65, edited by F. Sanso and R. Rummel, pp. 312–358, Springer, New York.

Tapley, B. D., S. Bettadpur, J. C. Ries, P. F. Thompson, and M. M. Watkins (2004), GRACE measurements of mass variability in the Earth system, *Science*, *305*, 503–505.

Torge, W. (1989), *Gravimetry*, Walter de Gruyter, New York.

Torge, W. (2001), *Geodesy*, 3rd ed., Walter de Gruyter, New York.

Tscherning, C. C., and R. H. Rapp (1974), Closed covariance expressions for gravity anomalies, geoid undulations and deflections of the vertical implied by anomaly degree variance models, in *Rep. No. 208*, Dept. of Geod. Sci. and Surv., The Ohio State Univ., Columbus, Ohio.

Verdun, J., E. E. Klingele, R. Bayer, M. Cocard, A. Geiger, and H. G. Kahle (2003), The alpine Swiss-French airborne gravity survey, *Geophys. J. Int.*, *152*, 8–19.

Wei, M., and K. P. Schwarz (1998), Flight test results from a strapdown airborne gravity system, *J. Geod.*, *72*, 323–332.

Wessel, P., and W. H. F. Smith (1999), *The Generic Mapping Tools (GMT), Technical Reference and Cookbook*, Univ. of Hawaii, Hawaii, USA.

Yen, H. Y., Y. H. Yeh, C. H. Lin, G. K. Yu, and Y. B. Tsai (1990), Free-air gravity map of Taiwan and its applications, *Terr. Atmos. Ocean. Sci.*, *1*, 143–156.

Yen, H. Y., Y. H. Yeh, and F. T. Wu (1998), Two-dimensional crustal structures of Taiwan from gravity data, *Tectonics*, *17*(1), 104–111.

K.-H. Chen, Department of Real Estate and Built Environment, Taipei University, No. 67, Sec. 3, Ming-Shen E. Road, Taipei, Taiwan.

R. Forsberg and A. V. Olesen, Danish National Space Center, Juliane Maries Vej 30, DK-2100, Copenhagen, Denmark.

Y.-S. Hsiao, C. Hwang, and H.-C. Shih, Department of Civil Engineering, National Chiao Tung University, 1001 Ta Hsueh Road, Hsinchu, Taiwan. (hwang@geodesy.cv.nctu.edu.tw)

M. Yang, Department of Geomatics, National Cheng Kung University, 1 Ta Hsueh Road, Tainan, Taiwan.